PCCP

Accepted Manuscript

ROYAL SOCIETY OF CHEMISTRY

www.rsc.org/pccp

Physical Chemistry Chemical Physics

ARTICLE

Atomic-Scale Insights into Structural and Thermodynamic Stability of Pd–Ni Bimetallic Nanoparticles

Received 00th January 20xx,
Accepted 00th January 20xx

DOI: 10.1039/x0xx00000x

www.rsc.org/

Rao Huang,[a] Yu-Hua Wen,*[a] Zi-Zhong Zhu[a] and Shi-Gang Sun[b]

Atomic–scale understanding of structures and thermodynamic stability of core–shell nanoparticles is of importance to both their syntheses and applications. In this article, we systematically investigated the structural stability and thermodynamic evolution of core–shell structured Pd–Ni nanoparticles by molecular dynamics simulations. It has been revealed that the dislocations and stacking faults occur in the shell and their amounts are strongly dependent on core/shell ratios. The presence of these defects lowers structural and thermal stability of these nanoparticles, resulting in even lower melting points than both Pd and Ni monometallic ones. Furthermore, different melting behaviors have been disclosed in Pd–core/Ni–shell and Ni–core/Pd–shell nanoparticles. The diverse behaviors cause different relationships between the melting temperature and the amounts of stacking faults. Our results display the direct evidence for the tunable stability of bimetallic nanoparticles. This study provides a fundamental perspetive on core–shell structured nanoparticles and has important implications for further tailoring their structural and thermodynamic stability by core/shell ratio or composition controlling.

1 Introduction

In the rapidly expanding field of nanocatalysis, bimetallic nanoparticles (NPs) have been extensively investigated in the past decades because of their enhanced catalytic properties and durability compared with their monometallic counterparts[1]. Among the most active transition metals, group VIII metals of Pd and Ni are particularly attractive for their excellent performances in widespread occasions such as electro–oxidations[2–4] for fuel cell applications, selective hydrogenation[5] and numerous cross–coupling reactions[6,7] for organic synthesis, catalytic conversion of exhaust gases[8,9], and so on. In these reactions, the improved selectivity and activity have been observed when Pd and Ni are in contact. This bimetallic synergetic effect, which is originated from the change in electronic structure of the coordinatively unsaturated atoms after alloying, has also been theoretically confirmed. For example, the density functional theory (DFT) calculations were conducted to investigate the *d*–band center shift and the segregation energy of transition metal alloys, and predicted that Pd–Ni alloys would exhibit high ethanol oxidation reaction (EOR) activity.[10]

As is known, the chemical and physical properties of core–shell NPs strongly depend on their architectures including structures, composition and morphology. For Pd–Ni or Ni–Pd core–shell NPs, due to the considerable difference of lattice constants between Pd and Ni (the lattice constant is 3.891 and 3.524 Å for Pd and Ni, respectively[11]), Pd lattice tends to endure compressive strain while Ni lattice tensile strain correspondingly in order to accommodate the core–shell interface. This strain field will unavoidably influence their structures and performances[12]. Although the formation of dislocations has been observed in Pd-Ni bimetallic core–shell NPs both experimentally[5, 13] and theoretically[14], there are still some important issues remain unclear. For examples, how does the amount of these defects depend on the composition or core/shell ratio? What will happen when the components of core and shell are exchanged? The clarification of these questions should be helpful for understanding the structure–property relationship of core–shell NPs.

Besides, the thermodynamic stability of core–shell NPs is crucial for their syntheses and practical applications because of two main aspects. On one hand, high–temperature treatments, such as solid metallurgy or thermal annealing, can be frequently involved in certain synthesizing procedures of these bimetallic NPs[15]. However, they tend to aggregate into larger ones when the ambient temperature reaches or exceeds the Tammann temperature[16]. Therefore, insights into their thermodynamic stability are of particular importance to preventing their sintering and coarsening. On the other hand, the catalytic activities of these core–shell NPs are strongly dependent on their structures (especially surface structures) and compositions distributions. When they are utilized in catalytic reactions taking places in high–temperature conditions (for example, in the cracking of petroleum or the purification of automobile exhaust gases), their structures and composition distributions could be significantly varied with the rising temperature due to the differences of components in cohesive energy, surface energy, atomic radius, diffusivity and so on.

[a] Institute of Theoretical Physics and Astrophysics, Department of Physics, Xiamen University, Xiamen 361005, China
Email: yhwen@xmu.edu.cn
[b] State Key Laboratory of Physical Chemistry of Solid Surfaces, Department of Chemistry, Xiamen University, Xiamen 361005, China

Consequently, their catalytic activities will rely heavily on the thermodynamics of the miscibility and segregation process of the components. To maintain the activities of these core–shell nanocatalysts at high temperatures, it is also necessary to obtain a thorough understanding of their thermodynamic behaviours.

Based on these aforementioned considerations, we conducted an atomistic investigation on structural stability and the thermodynamic behaviours of Pd–Ni bimetallic NPs. Different core/shell ratios were modelled to trace the compositional effects on the structures and stability. The evolutions of microstructure, energy and stress at different temperatures were examined. The article is organized as follows. A brief description of the simulation methodology is given in Section 2. The calculated results and discussion are presented in the third section. The main conclusions are summarized in the fourth section.

2 Computational Method

2.1 Model Construction

Two types of NPs, i.e., Ni–core/Pd–shell (denoted as Ni@Pd) and the inverted Pd–core/Ni–shell (denoted as Pd@Ni) NPs were constructed from a large face–centered cubic (*fcc*) single crystal, as seen in Figure 1. To facilitate a comparison study among different core/shell ratios, the total number of atoms in each NP was equally set at 44 843, corresponding to a particle diameter of about 9.5 nm. This particle size is significantly larger compared with the models in existing simulations on metallic NPs and closer to the experimental products.

2.2 Potential Description

On the basis of our previous works[17-20], the quantum corrected Sutton–Chen (Q–SC) type potentials were adopted to describe the interatomic interactions[21]. These potentials represent many–body interactions, and their parameters were optimized according to the lattice parameter, cohesive energy, bulk modulus, elastic constants, phonon dispersion, vacancy formation energy, and surface energy, resulting in an accurate description of thermodynamic and transport properties of metals and their alloys[22-24]. The total potential energy for a system of atoms can be expressed as

$$U = \sum_i U_i = \sum_i \varepsilon \left[\frac{1}{2} \sum_{j \neq i} V(R_{ij}) - c\sqrt{\rho_i} \right], \quad (1)$$

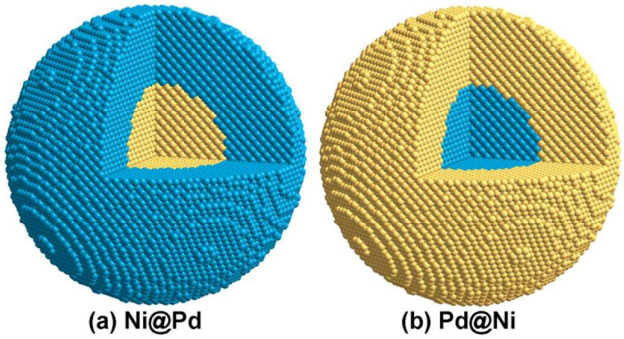

Fig. 1 Schematic illustration of (a) Ni@Pd and (b) Pd@Ni NPs. Coloring denotes type of atom: yellow, Ni atom; blue, Pd atom.

in which $V(R_{ij})$ is a pair interaction function defined by the following equation

$$V(R_{ij}) = \left(\frac{a}{R_{ij}} \right)^n, \quad (2)$$

accounting for the repulsion between the *i* and *j* atomic cores; ρ_i is a local electron density accounting for cohesion associated with atom *i* defined by

$$\rho_i = \sum_{j \neq i} \left(\frac{a}{R_{ij}} \right)^m. \quad (3)$$

In Equation (1)–(3), R_{ij} is the distance between the i_{th} and the j_{th} atoms; *a* is a length parameter scaling all spacings; *c* is a dimensionless parameter scaling the attractive terms; *ε* sets the overall energy scale; *n* and *m* are integer parameters. The model parameters for Ni and Pd are listed in Table 1. In order to describe the interatomic action between Ni and Pd, the geometric mean was used to obtain the energy parameter *ε* while the arithmetic mean was used for the remaining parameters[23,24].

Component	*n*	*m*	*ε*(*meV*)	*c*	*a* (Å)
Ni	10	5	7.3767	84.745	3.5157
Pd	12	6	3.2864	148.205	3.8813

Table 1 Potential parameters used in atomistic simulations for Pd–Ni bimetallic NPs [21].

2.3 Simulation Processing

Upon starting molecular dynamics (MD) simulations, all NPs were first quasi–statically relaxed to a local minimum energy state through the conjugate gradients method[25]. After full relaxation, these NPs were subjected to a continuous heating process. To make the simulations more realistic, constant temperature and pressure molecular dynamics (NPT–MD) were employed to allow energy and volume fluctuations, which may be critical to the resulting dynamics. These NPs underwent a heating process composed of a series of NPT–MD simulations from 0 to 1800 K with a temperature increment of 50 K. However, a smaller step of 10 K was adopted to examine the melting behavior more accurately when the temperature was close to the melting point. At each temperature, the MD simulations were carried out for 200 *ps*, during which atomic coordinates, velocities, and energies were extracted for calculation of the statistical quantities in the last 25 *ps*. The desired temperature and ambient pressure were maintained by Nose–Hoover thermostat[26] and Berendsen approach[27], respectively. The equations of atomic motion were integrated by the Verlet–velocity algorithm[28] with a 1 *fs* time step.

3. Results and Discussion

3.1 Structural Stability

The structural stability of materials with different structures can be estimated by the summation of the potential energy of each atom at ground state since the kinetic energies are zero. The criterion suggests that the structure with lower energy tends to be more stable. To highlight the role of the core–shell interface in

determining the structural stability of Pd–Ni bimetallic NP, monometallic Ni and Pd NPs with the same atomic number were also constructed for a comparison. Here, a common definition of Δ*E* has been introduced as follow

$$\Delta E = \sum_{i=1}^{N} E(i) - \sum_{j=1}^{N_{Ni}} E_{Ni}(j) - \sum_{k=1}^{N_{Pd}} E_{Pd}(k), \quad (4)$$

where N is the total atomic number of the system; N_{Ni} and N_{Pd} are respectively the atomic numbers of Ni and Pd atoms in the bimetallic NP; $E(i)$ represents the potential energy of atom i in the bimetallic NP; $E_{Ni}(j)$ and $E_{Pd}(k)$ respectively represent the potential energies of the j_{th} Ni and k_{th} Pd atoms in the corresponding monometallic NP with the identical positions in the bimetallic one. Therefore, Δ*E* is completely contributed by the introduction of the core–shell interface into bimetallic NPs.

The composition dependence of Δ*E* for Ni@Pd and Pd@Ni NPs has been displayed in Figure 2. Clearly, according to the definition of Δ*E*, if the value of *ΔE* is negative, it means that the structural stability of the bimetallic NPs is enhanced comparing with the monometallic ones. In contrast, all the results of *ΔE* in Figure 2 are positive, indicating that the existence of core–shell interface decreases the structural stability. Additionally, as shown in Figure 2, the values of Δ*E* are generally larger in the Pd@Ni NPs than in the Ni@Pd ones under the same core/shell ratios, suggesting that the decrease of structural stability aroused by the core–shell interface is more remarkable in the Pd@Ni NPs. Furthermore, it should be noted that the bimetallic NPs will evolve into monometallic ones when the core/shell ratio is 0 or ∞, where Δ*E* goes to zero. Therefore, both curves present the same tendency with the rising core/shell ratio: They increases firstly and decreases subsequently, as shown in Figure 2. Δ*E* reaches the maximum at the core/shell ratio of 2/1 and 8/1 for the Ni@Pd and Pd@Ni NPs, respectively, signifying that the existence of the interface has the strongest effect on structural stability at the corresponding ratio.

As mentioned in Section 1, considerable internal strain/stress will be built up around the interface due to the large difference of lattice constants between Ni and Pd. In order to further investigate

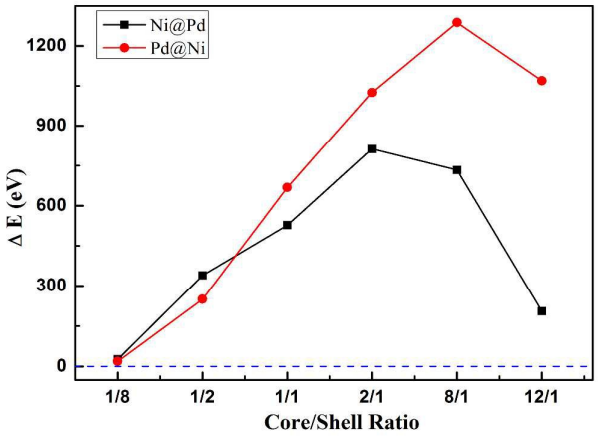

the influence of the introduction of the core–shell interface on the NPs, we calculated the local stress in the two bimetallic NPs. The local stress σ_n at the i_{th} atom site can be written as

Fig. 2 Composition dependent Δ*E* of two types of Pd–Ni bimetallic NPs.

$$\sigma_n = \frac{1}{3}\sum_{\alpha=1}^{3}\sigma_{\alpha\alpha} = \frac{1}{3}\sum_{\alpha=1}^{3}\left(\frac{1}{2\Omega_i}\sum_{j\neq i}F_{ij}^{\alpha}R_{ij}^{\alpha}\right), \quad (5)$$

where F_{ij} and R_{ij} are the force and distance between atoms i and j.[29] Ω_i is the local volume that can be identified with the volume of the Voronoi polyhedra constructed by the perpendicular planes that bisect the lines between atom i and all its neighbour atoms.[17]

Figure 3 demonstrates the stress distributions in bimetallic NPs with different core/shell ratios. Evidently, atoms in the Ni core basically possess positive values, indicating tensile stress. In contrast, atoms in the Pd core always present negative values, suggesting that they are under compressive stress. This result can be solely attributed to the fact that Ni has a much small lattice constant (3.524 Å) comparing with Pd (3.891 Å). Meanwhile, it is observed that under the same core/shell ratio, the absolute value of the stress in Pd core is larger than that in Ni core.

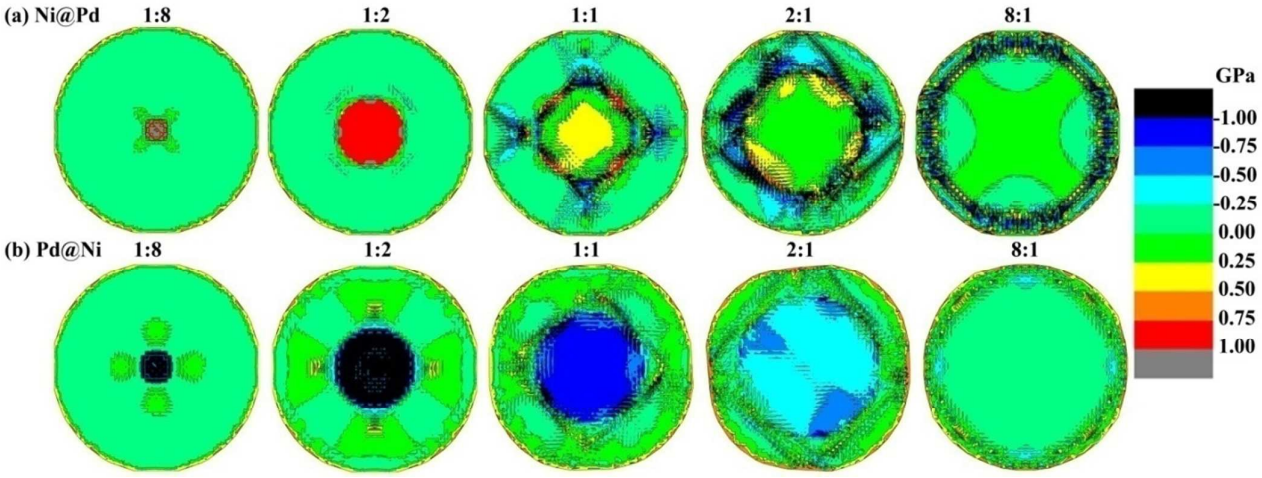

Fig. 3 Stress distributions in the cross–section of (a) Ni@Pd and (b) Pd@Ni NPs with different core–shell ratios at ground state.

Physical Chemistry Chemical Physics

ARTICLE

Furthermore, the stresses in the cores of the two types of NPs both reduce as the core sizes grow. This reason is that the lattice misfit only occurs at the core–shell interface, and the ratio of the interface area to the core volume remarkably decreases with the core size rising, thus weakening the effects of the lattice misfit on the entire core. In addition, the symmetry of the stress distribution is broken at medium core/shell ratios such as 1:1 and 2:1, as depicted in Figure 3. This phenomenon can be attributed to the appearance of dislocations and stacking faults which destroy the symmetry of the original atomic arrangement in the particle. It is worth noting that for both types of bimetallic core–shell NPs, the dislocations and stacking faults are generally distributed in the shell and terminated at the interface and surface, in agreement with our previous study.[17] Therefore, these defects are not formed when the core size is relatively small (see the core/shell ratio=1:8 or 1:2 in Figure 3), since the effect of lattice misfit at interface on the shell is insufficient. As for the NPs with the largest core/shell ratio (8:1), the stress distributions seem roughly symmetric. The dislocations or stacking faults cannot be confirmed merely from the corresponding snapshots. However, the symmetric distribution of stress can be easily understood even for the existence of dislocation: As the ratio of the interface area to the core volume reaches the largest value, the effects of the lattice misfit at interface on the entire core are correspondingly minimized. Therefore, these defects are not able to cause unsymmetry of stress distribution.

3.2 Thermodynamic Stability

For the purpose of exploring the thermodynamic stability of Pd–Ni bimetallic NPs, some important information concerning the thermodynamic properties, the characteristics and progress of melting during the heating process should be firstly extracted from data records of MD simulations. Experimentally, the usual way to study the phase transition is to investigate the caloric curve (energy versus temperature) of the system.[30] To identify the critical temperature of solid–liquid phase transition, an effective and feasible method is to monitor the change in the thermodynamic properties such as total energy and specific heat capacity. Note that the specific heat capacity can be deduced from temperature–dependent potential energy according to the following equation[22]

$$C_p(T) = \frac{dU}{dT} + \frac{3}{2}R_{gc}, \qquad (6)$$

where U is potential energy, and R_{gc}=8.314 J/(molK). The phase transition occurs at the temperature where the potential energy shows an abrupt peak and the heat capacity accordingly displays a sharp rise.

As a representative, the temperature-dependent potential energies of the two types of bimetallic NPs with core/shell ratio of 1:1 are demonstrated in Figure 4. It is clearly seen from this figure that the potential energy increases almost linearly at low temperatures, followed by an abrupt rising at the melting point (T_m). According to the peaks of heat capacity, it can be ascertained that the T_m of the Ni@Pd and Pd@Ni NPs are 1430 K and 1330 K, respectively. In our previous studies, two prominent peaks have been usually observed in caloric curves of Pt-Pd and Pt-Au core–shell NPs, indicating the "two–stage" melting.[18,19] However, in the current Pd-Ni system, there exists only one distinct peak in each curve, presenting a caloric curve similar to that of monometallic NPs. This can be attributed to the fact that a typical "two–stage" melting only occurs when a considerable difference of T_m exists between the two components in core–shell NPs. For example, the melting points of bulk Pt, Pd, Au and Ni are respectively 2045, 1827, 1338 and 1728 K[11]. The differences of T_m between components in Pt-Pd and Pt-Au bimetallic NPs are respectively 218 and 707 K. In contrast, the difference between Pd and Ni (99 K) is relatively small, thus the "two–stage" melting phenomenon is absent in Pd–Ni bimetallic NPs.

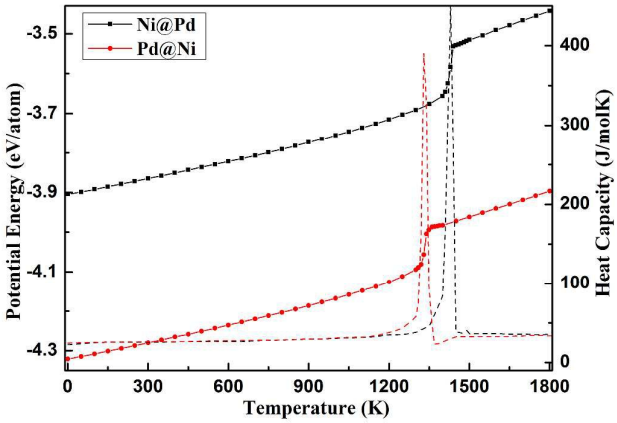

Fig. 4 Temperature dependence of potential energy (solid lines) and the corresponding heat capacities (dashed lines) for the two types of NPs with the core/shell ratio of 1:1.

According to the caloric curves of the NPs, we may deduce their melting points under different compositions (*i.e.*, different core/shell ratios), as illustrated in Figure 5. In our previous studies, the melting temperatures of Au–Pd and Pt–Pd bimetallic NPs generally lie between those of the corresponding monometallic ones and monotonically vary with composition.[17,18] In this work, however, the melting points of Pd–Ni core–shell NPs under most compositions are even lower than the T_m of pure Ni NP (1370 K). Furthermore, the melting points firstly decrease and subsequently increase with rising core composition, displaying a feature of non-monotonicity. Comparing the structures of Pd–Ni bimetallic NPs with Au–Pd and Pt–Pd ones, one significant difference is that the

defects such as dislocations or stacking faults exist in the former but are absent in the latter. We believe that the existence of these defects may be responsible for the abnormal dependence of the melting point on composition.

To obtain an in-depth understanding of this unusual composition dependence of thermal stability of Pd–Ni bimetallic NPs, we examined their structural evolutions during continuous heating. Here, the common neighbour analysis (CNA), proposed by Honeycutt and Andersen,[31] was employed to characterize the local crystal structure. This method has already been extensively adopted to analyze the structural evolution of nanomaterials during the mechanical deformation and melting process[32,33]. To determine the crystal structure, the bonds between an atom and its nearest neighbours were examined. Utilizing this analysis, all the atoms in a NP were classified into three categories: Atoms in a local *fcc* order were considered to be *fcc* atoms; Atoms in a local hexagonal close packing (*hcp*) order were classified as *hcp* atoms, whose occurrence in an *fcc* crystal is generally regarded as the structure of stacking faults caused by the activities of Shockley partial dislocations; Atoms in all other local orders were considered to be "other" atoms since they did not reveal any useful information in *fcc* NPs.

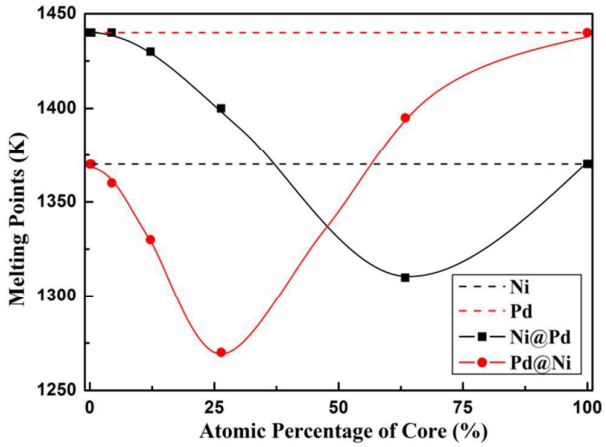

Fig. 5 Composition dependent melting points of the two types of bimetallic NPs (solid lines), in comparison with their monometallic counterparts (dashed lines).

Since the existence of stacking faults can be considered as a criterion to experimentally identify the formation of some core–shell structures[12], the statistic of their amounts is necessary. Figure 6 displays atomic percentages of *hcp* atoms in the shells of both types of NPs with rising temperature. Considering that the curves for different compositions are essentially analogous, the results of NPs with core/shell ratio of 1:1 are presented as a representative. Clearly, the number of *hcp* atoms decreases continuously until falls to zero around the melting point. As can be seen from Figure 6, a significant number of stacking faults occur at 0 K in both the Ni@Pd and Pd@Ni NPs, which confirmed the earlier discussion of Figure 3. Such numerous stacking faults would definitely affect the thermal stability of the NPs. Accordingly, it is not surprising that the melting points of the NPs with some core/shell ratios obviously drop to even lower than 1370 K (see Figure 5). Meanwhile, the composition dependent percentages of *hcp* atoms at room temperature of 300 K are displayed in the inset of Figure 6. Evidently, there exists a maximum in percentages of *hcp* atoms at core composition of 26.4% (corresponding to the core/shell ratio of 2:1) for both types of NPs. Naturally, it is reasonable to expect that the lowest melting temperatures should occur in the NPs with the maximum *hcp* atoms. It is found that this assumption is valid for the Pd@Ni NPs, in which the lowest T_m indeed appears at core composition of 26.4% (see Figures 5 and 6). However, for the Ni@Pd ones, the lowest T_m does not appear at this composition, but happens at the core composition of 63.4% (see Figure 5). This indicates that the melting point is not simply determined by the quantities of stacking faults but also associated with other factors such as the different melting processes in these two types of NPs.

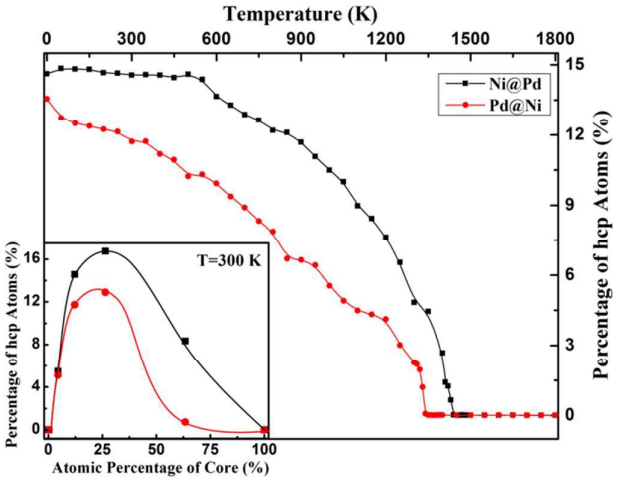

Fig. 6 Temperature dependent percentage of *hcp* atoms in the shells of two types of bimetallic NPs with core/shell ratio of 1:1. (Inset) Composition dependent percentage of *hcp* atoms at room temperature of 300 K.

For thoroughly examining the melting mechanisms of these two types of bimetallic NPs, here we introduce the bond order parameter method[34] to distinguish between atoms in solid and liquid environments during the melting. To determine the orientational order, spherical harmonic basis functions $Y_{lm}(\mathbf{r}_{ij})$ are associated with every bond joining an atom to its near neighbours. The term "bond", which does not correspond to conventional chemical bond, refers to the unit vector $\mathbf{r}_{ij}$ connecting a reference atom *i* with its neighbour atom *j* that are within a given radius of cutoff distance. The local order around the atom *i* is defined by:

$$q_{lm}(i)=\frac{1}{N_{nb}(i)}\sum_{j=1}^{N_{nb}(i)}Y_{lm}(\mathbf{r}_{ij}). \quad (7)$$

Meanwhile, only even–*l* spherical harmonics, which are invariant under inversion, were considered. For symmetry reasons, the first nonzero value occur for *l*=4 in clusters with cubic symmetry and for *l*=6 in clusters with icosahedral symmetry. Therefore, *l*=6 is restricted to be an index to distinguish various solid structures from the liquid, which can be realized by comparing the values of $q_{6m}(i)$ with those of the nearest neighbours. This is done by using a normalized $(2\times 6+1)$–dimensional vector $\hat{q}_6(i)$, with components

$$\hat{q}_{6m}(i)=\frac{q_{6m}(i)}{\sqrt{\sum_{m=-6}^{6}q_{6m}(i)q_{6m}^{*}(i)}} \quad (8)$$

Physical Chemistry Chemical Physics

ARTICLE

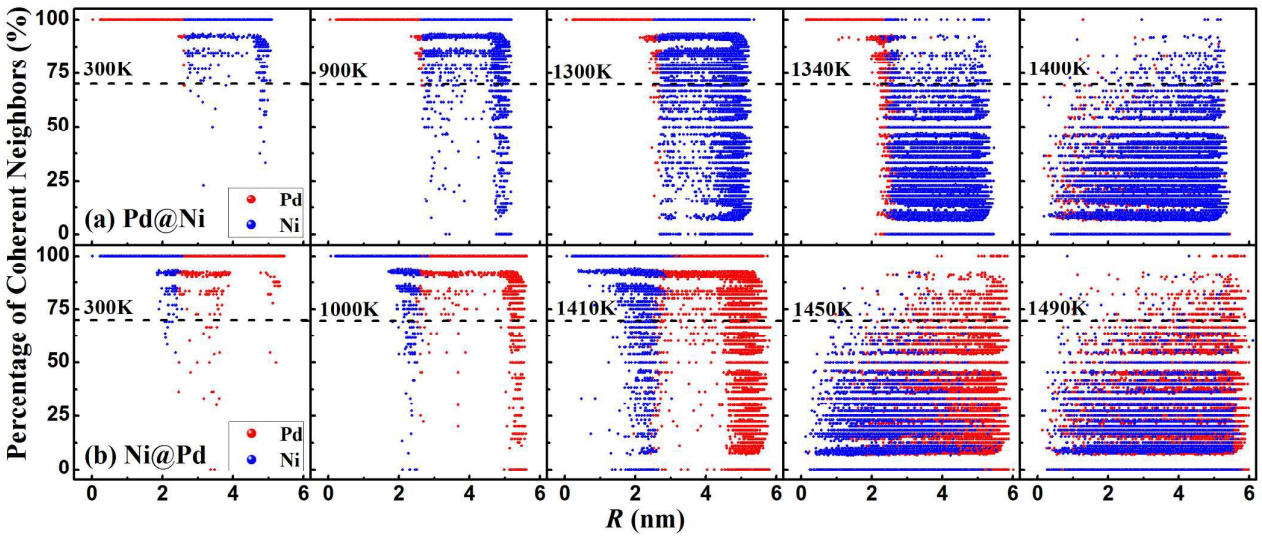

Fig. 7 Distributions of percentage of coherent neighbors at representative temperatures for (a) Pd@Ni and (b) Ni@Pd NPs with core/shell ratio of 1:1. The dashed line denotes the criterion value of 70%. Note that the horizontal axis denotes the distance between the atom and the particle center of mass.

and a dot product of the vectors $\hat{q}_6$ of neighbouring atoms *i* and *j* is computed as:

$$s_6(i,j) = \sum_{m=-6}^{6} \hat{q}_{6m}(i)\hat{q}^*_{6m}(j), \quad (9)$$

The atom *i* and *j* are called "coherent" if s_6>0.5. This criterion allows for a good separation of solid– and liquid–like atoms: the atom is defined as being solid–like if it is coherent with more than 70% of its neighbors.[35]

Figure 7 presents the distribution of percentages of coherent neighbours at five temperatures in both types of bimetallic NPs with core/shell ratio of 1:1. According to the bond order parameter method, it is obvious that those points above the dashed line indicate solid atoms, while those below signify liquid ones. One can see that at room temperature of 300 K, 99.92% atoms in the particle are solid. Hence, the bond order parameter method should be reliable in discriminating between the solid and the liquid atoms. It can be seen that the two NPs exhibit different melting behaviours by comparison of Figure 7a and 7b. For the Pd@Ni NP, the premelting starts from surface at around 900 K, and gradually extends into the core region. At 1340 K, the liquid atoms begin to appear at the outer layer of the core, and most atoms in the shell have already melted (see Figure 7a). Generally, the melting of the Pd@Ni NP progresses homogenously from the surface into the interior, similar to that of the monometallic NPs.[22] However, for the inverted Ni@Pd NP, the outer layer of the core melts almost simultaneously with the particle surface, as seen in the snapshots of 1000 and 1410 K in Figure 7b. The simultaneous melting and development of core and shell have usually happened in NPs whose core component have a melting point distinctly lower than the shell.[36] From these two diverse melting modes aforementioned, it can be explained why the lowest melting temperature does not occur at the composition with the largest number of stacking faults in both types of NPs. As is known, the premelting temperature of NP has a decisive influence on its overall melting temperature. For the Pd@Ni NP, the melting is triggered by the premelting of the shell, and the core does not melt until the entire shell turns into liquid. Since all the stacking faults are distributed in the shell, the more stacking faults thus directly result in the lower T_m of the whole particle. For the inverted Ni@Pd NP, however, the outer layers of the core generally melt prior to the interior region of the shell (see Figure 7b), suggesting that the premelting of the core also plays a significant role in determining the overall melting point. Consequently, the Ni@Pd NP with a larger core size (core composition of 63.4%) may present an even lower T_m comparing with the one with a smaller core size but more stacking faults (core composition of 26.4%).

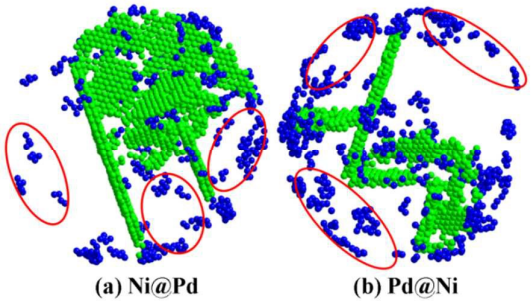

Fig. 8 Snapshots of liquid atoms and the stacking faults in the (a) Ni@Pd and (b) Pd@Ni NPs at the temperature where the premetling originates (respectively 1100 and 950 K).

In order to further ascertain the influence of stacking faults on the melting process, two snapshots were extracted from MD simulations to display the distribution of liquid atoms and the stacking faults at the temperature where the premelting starts, as shown in Figure 8. Apparently, the premelting does not necessarily happen near the stacking faults (see those atoms in the red circles). It may be deduced from this figure that the existence of dislocations or stacking faults reduces the thermal stability of the NPs because they serve as interior defects in the system thus accelerate the progress of melting, rather than contribute to the premelting at the surface.

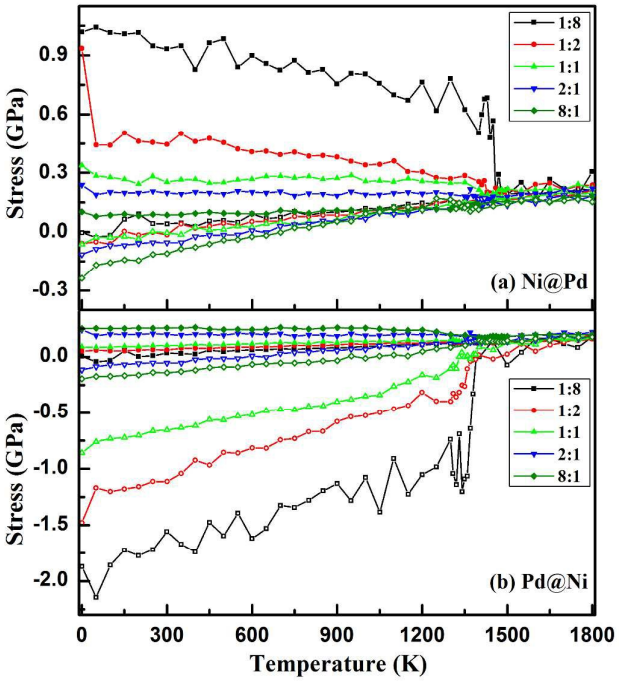

Fig. 9 The average stress of the two components in (a) Ni@Pd and (b) Pd@Ni NPs with different core/shell ratios during continuous heating. The solid symbols denote the results of Ni atoms, and the hollow symbols represent those of Pd atoms.

Finally, we calculated the average stress of the two components in these bimetallic NPs with different core/shell ratios during continuous heating, as demonstrated in Figure 9. A most remarkable characteristic is that for both types of NPs, the gap between the tensile stress of Ni atoms and the compressive stress of Pd atoms basically decreases with rising temperature, and eventually tends to be zero beyond overall melting. This decrease of stress gap should be mainly associated with different thermal expansion coefficients between the core and shell. The linear coefficient of thermal expansion is 13.4×10^{-6} K^{-1} for Ni and 11.8×10^{-6} K^{-1} for Pd[37], respectively, meaning that Ni lattice expands relatively faster than Pd lattice. Considering that Ni has smaller lattice constant than Pd, it is natural to find that the stress gap aroused by the lattice misfit between Ni and Pd will reduce with elevating temperatures. Furthermore, it is also noted that the stress in the shells of the two NPs with core/shell ratio of 1:2 present a distinct step change when the temperature is increased from zero to 50 K. According to the statistics of *hcp* atoms in these two corresponding NPs, the stacking faults are not formed at ground state, while they emerge at the temperature of 50 K. It indicates that the stress, accumulated in the NPs, may be released by the nucleation and activities of dislocations, resulting in the formation of stacking faults and the appearance of *hcp* atoms. Since the stress gap is reduced in succession with rising temperature, this could be the reason that the numbers of stacking faults in these NPs continuously decrease. Interestingly, the opposite case was found in our previous study that numerous stacking faults were generated in Au–Pt bimetallic NPs with continuously heating.[19] This different situation should be attributed to the larger lattice constant of Au (4.08 Å) than that of Pt (3.92 Å)[11] and meantime the larger linear thermal expansion coefficient of Au (14.2×10^{-6} K^{-1}) than that of Pt (8.8×10^{-6} K^{-1}).[37] Consequently, the stress gap between the two components will increase with rising temperature, leading to the formation of more stacking faults. Therefore, the temperature dependence of the amount of stacking faults is closely related to both lattice constants and thermal expansion coefficients of the components. This observation may be broadened to all the other core–shell bimetallic NPs.

4. Conclusions

In summary, molecular dynamics simulations were employed to explore the structural stability and thermodynamic behaviours of Ni@Pd and Pd@Ni NPs. The common neighbour analysis was adopted to identify the stacking faults, and the bond order parameters were introduced to disclose the melting mechanism. The stress distribution and its temperature dependence were also examined. The major conclusions are listed as follows.

(1) The existence of core–shell interface decreases the structural stability of Pd–Ni bimetallic NPs. In comparison, the decrease of structural stability is more remarkable in Pd@Ni NPs. Meanwhile, considerable stress gaps exist at the core–shell interface in both types of NPs, which is resulted from the relatively large lattice misfit between the two elements. These stress gaps induce the generation of stacking faults, whose amounts are dependent on core/shell ratios.

(2) Attributed to the existence of stacking faults, the melting points of Pd–Ni bimetallic NPs can be brought down to even lower than those of pure Pd and Ni NPs. Moreover, the "two–stage" melting does not happen in Pd–Ni bimetallic NPs owing to the relatively close melting points of Pd and Ni. Nevertheless, different melting behaviours have been discovered in Ni@Pd and Pd@Ni NPs despite that their caloric curves are similar to those in monometallic NPs. The diverse melting behaviours lead to different relationships between the melting temperature and the amount of stacking faults. Besides, the stacking faults, as interior defects in the system, accelerate the development of melting rather than contribute to the premelting at the surface.

(3) The amount of stacking faults continuously decreases with elevating temperatures, which is attributed to the reduced stress gap between core and shell. The temperature dependent behavior has been determined by both lattice constants and thermal expansion coefficients of the components.

These results provide important insights into rich diversity of compositional properties of Pd–Ni bimetallic NPs at atomistic level. Some conclusions can also be applicable to other bimetallic even

multi-metallic core–shell structured NPs. The current study is expected to provide a systematic basis not only to syntheses of NP catalysts but also to further design of novel nanostructures with both excellent performance and enhanced stability.

Acknowledgements

This work was supported by the National Natural Science Foundation of China (Grant Nos. 51271156 and 11204252), the Natural Science Foundation of Fujian Province of China (Grant No. 2013J06002), the Specialized Research Fund for the Doctoral Program of Higher Education of China (Grant No. 20130121110012), and the Fundamental Research Funds for the Central Universities of China (Grant No. 20720150023).

Notes and references

1 R. Ferrando, J. Jellinek and R. L. Johnston, *Chem. Rev.*, 2008, **108**, 845.
2 Y. Zhao, X. Yang, J. Tian, F. Wang and L. Zhan, *Int. J. Hydrogen Energy,* 2010, **35**, 3249.
3 Z. Zhang, L. Xin, K. Sun and W. Li, *Int. J. Hydrogen Energy,* 2011, **36**, 12686.
4 Y. She, Z. Lu, W. Fan, S. Jewella and M. K. H. Leung, *J. Mater. Chem. A,* 2014, **2**, 3894.
5 R. Massard, D. Uzio, C. Thomazeau, C. Pichon, J. L. Rousset and J. C. Bertolini, *J. Catal*., 2007, **245**, 133.
6 Ö. Metin, S. F. Ho, C. Alp, H. Can, M. N. Mankin, M. S. Gültekin, M. Chi and S. Sun, *Nano Res.,* 2013, **6**, 10.
7 L. Feng, H. Chong, P. Li, J. Xiang, F. Fu, S. Yang, H. Yu, H. Sheng and M. Zhu, *J. Phys. Chem. C,* 2015, **119**, 11511.
8 Y. Hillia, N. M. Kinnunena, M. Suvantoa, A. Savimäkib, K. Kallinenb and T. A. Pakkanen, *Appl. Catal. A,* 2015, **497**, 85.
9 J. Shen, R. E. Hayes, X. Wu and N. Semagina, *ACS Catal.,* 2015, **5**, 2916.
10 U. B. Demirci, *J. Power Sources,* 2007, **173**, 11.
11 C. Kittel, *Introduction to solid state physics*, John Wiley & Sons, New York, USA, 1996.
12 B. T. Sneed, A. P. Young and C. K. Tsung, *Nanoscale*, 2015, **7**, 12248.
13 S. Sao-Joao, S. Giorgio, J. M. Penisson, C. Chapon, S. Bourgeois and C. Henry, *J. Phys. Chem. B*, 2005, **109**, 342.
14 K. D. Watson, S. E. Tatsinkou Nguelo, C. Desgranges and J. Delhommelle, *Crystengcomm*, 2011, **13**, 1132.
15 Y. Tang, S. D. Xu, Y. H. Dai, X. Q. Yan, R. H. Li, L. P. Xiao and J. Fan, *Chem.Commun.,* 2014, **50**, 213.
16 J. Sun, D. Ma, H. Zhang, X. Liu, X. Han, X. Bao, G. Weinberg, N. Pfänder and D. Su, *J. Am. Chem. Soc.,* 2006, **128**, 15756.
17 R. Huang, Y. H. Wen, G. F. Shao and S. G. Sun, *J. Phys. Chem. C,* 2013, **117**, 4278.
18 R. Huang, Y. H. Wen, Z. Z. Zhu and S. G. Sun, *J. Phys. Chem. C,* 2012, **116**, 11837.
19 R. Huang, G. F. Shao, X. M. Zeng and Y. H. Wen, *Sci. Rep.,* 2014, **4**, 7051.
20 R. Huang, G. F. Shao, Y. H. Wen and S. G. Sun, *Phys. Chem. Chem. Phys.,* 2014, **16**, 22754.
21 T. Cagin, K. Kimura, Y. Qi, H. Li, H. Ikeda, W. L. Johnson and W. A. Goddard, *Mater. Res. Soc. Symp. Proc.,* 1999, **554**, 43.
22 Y. Qi, T. Cagin, W, L. Johnson and W. A. Goddard, *J. Chem. Phys*., 2001, **115**, 385.
23 H. Ikeda, Y. Qi, T. Cagin, K. Samwer, W. L. Johnson and W. A. Goddard, *Phys. Rev. Lett.,* 1999, **82**, 2900.
24 S. K. R. S. Sankaranarayanan, V. R. Bhethanabotla and B. Joseph, *Phys. Rev. B,* 2005, **71**, 195415.
25 A. R. Leach, *Molecular modelling: principles and applications*, Pearson Education–Hall, London, UK, 2001.
26 D. L. Evans and B. L. Holian, *J. Chem. Phys.,* 1985, **83**, 4069.
27 H. J. C. Berendsen, J. P. M. Postma, W. F. van Gunsteren, A. DiNola and J. R. Haak, *J. Chem. Phys.,* 1984, **81**, 3684.
28 W. C. Swope, H. C. Anderson, P. H. Berens and K. R. Wilson, *J. Chem. Phys.,* 1982, **76**, 637.
29 C. Mottet, G. Rossi, F. Baletto and R. Ferrando, *Phys. Rev. Lett.,* 2005, **95**, 035501.
30 G. A. Breaux, C. M. Neal, B. Cao and M. F. Jarrold, *Phys. Rev. Lett.,* 2005, **94**, 173401.
31 J. D. Honeycutt and H. C. Andersen, *J. Phys. Chem.,* 1987, **91**, 4950.
32 J. Schiøtz, F. D. Di Tolla and K. W. Jacobsen, *Nature,* 1998, **391**, 561.
33 Y. H. Wen, Y. Zhang, J. C. Zheng, Z. Z. Zhu and S. G. Sun, *J. Phys. Chem. C,* 2009, **113**, 20611.
34 P. J. Steinhardt, D. R. Nelson and M. Ronchetti, *Phys. Rev. B* 1983, **28**, 784.
35 Y. Chushak and L. B. Bartell, *J. Phys. Chem. A,* 2000, **104**, 9328.
36 Y. H. Wen, R. Huang, C. Li, Z. Z. Zhu and S. G. Sun, *J. Mater. Chem.,* 2012, **22**, 7380.
37 D. R. Lide, (ed) *CRC handbook of chemistry and physics* (84_{th} Edition), CRC Press. Boca Raton, Florida, USA, 2003.

Graphic Abstract